Research article

Fracture behavior of additively manufactured corrax maraging stainless steel

Xiaojie Zhao [a], Yang Gao [a,b], Kai Zhao [a,**], He Liu [a,b]

[a] *PetroChina Research Institute of Petroleum Exploration & Development, Beijing, 100083, China*
[b] *National Key Laboratory of Continental Shale Oil, Da Qing, 163318, China*

ARTICLE INFO

ABSTRACT

Additively manufactured a low carbon Fe–Cr–Ni–Al Corrax stainless steel has ultra-high strength, but the mechanism at work when the steel cracks is still unclear. In this study, Corrax stainless steel was tensile tested to fracture and cracks in the vicinity of the fracture surface were analyzed by scanning electron microscope and electron-backscattered diffraction. The results show that the cracks propagated at angles of 45–60° to the tensile axis. Some cracks were transgranular, and high-angle grain boundaries had little effect on crack propagation. Crack propagation was inhibited in regions with lower Taylor factors. Kernel average misorientation value analysis established that the crack propagation process is accompanied by significant plastic deformation. The influence of particles and unfused pores on crack propagation is also discussed.

1. Introduction

CX (Corrax®) steel, as a low carbon maraging stainless steel, contains ~12 wt% Cr, 8~10 wt% Ni, ~1.4 wt% Mo and ~1.5 wt% Al that possesses excellent mechanical and chemical properties [1–3]. After proper heat treatment, almost no Cr-rich carbides or residual austenite remain in CX steel. This avoids the effect of phase boundaries on the stability of passive film. Hence, CX steel has better corrosion-resistance than AISI 420 stainless steel [4]. After aging, large numbers of uniformly distributed nanoscale-coherent β-NiAl particles form in CX stainless steel, giving extremely high strength [5–7]. This steel therefore has a wide range of potential applications in the energy, marine, chemical, and manufacturing industries.

Additive manufacturing is the usual method for manufacturing CX stainless steel components [8]. In additive manufacturing, complex three-dimensional components are directly fabricated layer by layer. Besides the manufacturing method [9], many other factors also affect the performance of CX stainless steel components. For example, the mechanical properties depend on the direction, often resulting in coarse grains and lower hardness along the printing direction [10]. This may be due to the existence of texture in the printed material, leading to anisotropy in mechanical properties [11]. Processing parameters, such as laser power and scanning speed, also have marked impacts on the properties [3]. Heat treatment also has a significant influence on the microstructure of CX stainless steel. An appropriate heat treatment process can refine martensite laths, retain a high dislocation density, reduce segregation, and generate large numbers of β-NiAl particles, thereby optimizing the performance of the components [12,13].

The microstructure of additively manufactured CX stainless steel is intricate, and its cracking behavior can be expected to be extremely complex [14–16]. Recent reports have shown that the broken surfaces of additively manufactured CX stainless steel exhibit

dimples characteristic of ductile fracture, with large voids and unmelted powder present on the tensile fracture surfaces [17–19]. However, the details of the cracking process and its mechanisms are still unclear. In this study, tensile tests were conducted on additively manufactured CX stainless steel and the cracking process analyzed by scanning electron microscope (SEM) and electron backscatter diffraction (EBSD) to reveal the cracking mechanism.

2. Material and methods

The material for testing was prepared using selective laser melting (SLM). The chemical composition of CX steel powder was (wt. %): 0.03C, 11.83Cr, 8.93Ni, 1.43Mo, 1.47 Al, 0.03Si, and the balance Fe. The printing equipment was a Resilience UM250 3D printer and the layer thickness, laser power, and scanning speed were 50 μm, 275 W, and 1200 mm/s, respectively. The billet was heated to 850 °C and held at that temperature for 30 min, followed by air quenching. After that, it was aged at 520 °C for 3 h. The heat treatment is a convenient method for obtaining dispersed precipitates, and eliminating residual stress, thereby improving the performance of SLM printed parts. An Axiover 200 MAT metallographic microscope(OM) and SU-5000 scanning electron microscope were used to examine the microstructures of the SLM CX stainless steel samples. Microstructures and crystallographic orientations were analyzed by electron-backscattered diffraction microscopy (EBSD). The scanning step length was 0.1 μm and the voltage was 30 kV. Nanostructures and nano-particles were characterized on a Talos transmission electron microscope (TEM). The tensile specimen was machined along the building direction on the aged billet. The gauge sections were $3 \times 2 \times 7$ mm. The dimension of tensile test specimens is shown in Fig. 1. Tensile tests were carried out on a MTS AG-X equipment at 25 °C and 0.03 mm/s. Three samples were tested to ensure repeatability. The fracture morphologies of the tensile were examined using SEM. The side surfaces of the fractured specimens were ground and then polished using 20 nm colloidal silica. The EBSD analysis of cracks near the fracture surface were performed using a ZEISS Gemini460 SEM with scanning steps of 0.05 μm and TSL–OIM–Analysis software.

3. Results

Fig. 2 shows the microstructure of SLM printed CX stainless steel under OM and SEM. After solution aging, the microstructure was homogenous and molten pool boundaries were difficult to identify (Fig. 2a). The microstructure of the steel showed abundant martensite (α phase). A small number of defects, especially inclusions and pores, can be detected in Fig. 2a-c marked by yellow arrows. Fine blocky grains and substructures were observed. The microstructure was further examined using EBSD. The results depicted in the inverse pole figure map (IPF) indicate that the crystallographic orientation of the SLM CX sample was random, and no texture was apparent (Fig. 2e). Grain size is a significant indicator revealing the mechanical properties of the steel. Fig. 2f presents the grain boundaries distribution. Blue and red lines represent high-angle and low-angle grain boundaries, respectively. The proportion of high-angle and low-angle grain boundaries is similar. Statistics show that the average effective grain size of CX stainless steel is 1.37 μm (Fig. 2g), with nearly 60 % of grains being less than 1 μm. The strain localization is characterized by kernel average misorientation (KAM) analysis. The percentage of KAM value for CX stainless steel that was less than 1° was 81 %, and the average KAM value was 0.75° (Fig. 2i).

Fig. 3 displays the TEM microstructures in the SLM CX stainless steel. The entanglement of dislocations around substructures was evident. Low-carbon martensite laths were obtained after the solution treatment of CX stainless steel. During the subsequent aging process at 520 °C, the alloying elements in the supersaturated solid solution easily segregate and accumulate at the dislocations and boundaries. When the composition fluctuation at these locations reaches the critical nucleation condition of precipitates, the precipitates begin to nucleate and grow. The highly dispersed nano-sized precipitates then strengthen the material (Fig. 3d).

Fig. 4 shows the stress-strain curve of the SLM CX stainless steel. The yield strength and ultimate tensile strength of CX stainless steel are 1602 MPa and 1647 MPa, respectively. As for the tensile performance, the SLM CX steel presented high strength because of the fine grains caused by extremely rapid cooling, high density dislocations and dispersed precipitates. The elongation of the CX stainless steel was 8.9 %.

Fig. 5 shows the fracture morphology of the tensile specimen, which consists of three parts, fibrous, radial and shear lip areas (Fig. 5b). The fibrous area, located in the center of the fracture, is the origin of the crack. The fracture morphology in fibrous and radial areas is composed of dimples and cleavage fractures, such as river-like patterns and tear ridges (Fig. 5f). The radial area followed by the fibrous area is the zone where the crack is transformed from slow expansion to fast and unstable expansion. Obvious secondary cracks and crystalline features are observed on the fracture surface(Fig. 5g). There is unfused powder at the edge of the radial area. Shear lip area is the last fracture area and there are many voids in this region (Fig. 5h). The fracture morphology in these three areas is different.
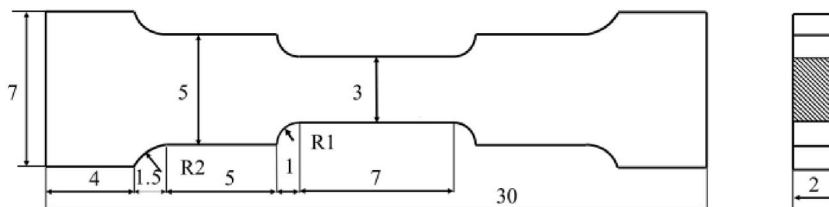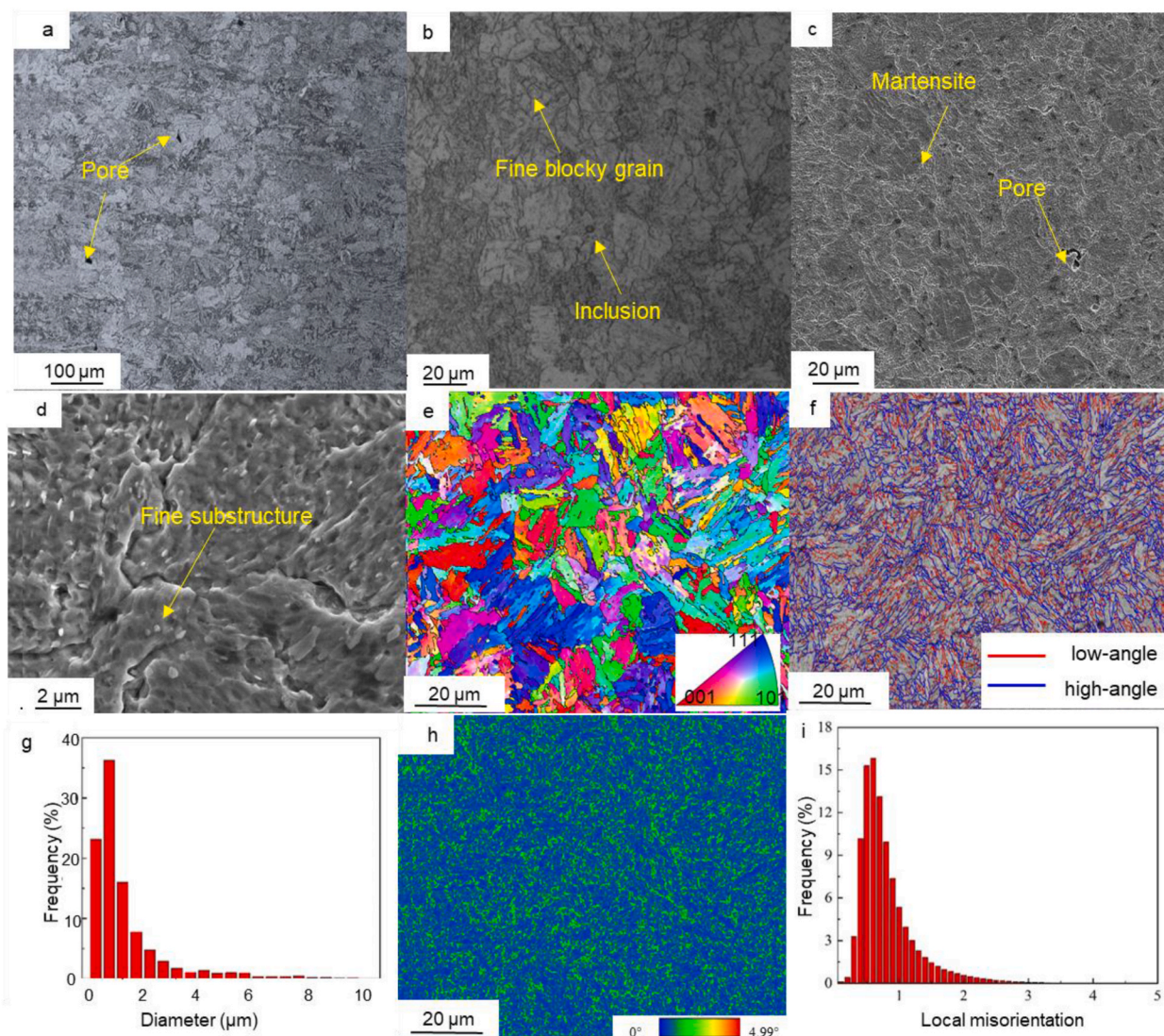

Fig. 1. Drawing of tensile specimen.

Fig. 2. Microstructures of SLM CX stainless steel: (a, b) OM images; (c, d) SEM images; (e) IPF images; (f, g) Grain boundary distribution; (h, i) KAM images.

The number of dimples in shear lip area was higher than those in radial and fibrous zones, and the number of cleavage fractures formed through the dimples in fibrous and radial zones was higher than those in shear lip zones. In general, the presence of secondary cracks and dimples indicates that the CX steel underwent significant plastic deformation. Stress concentration occurs at the inclusion, resulting in the nucleation and growth of microvoids (Fig. 5i). As shown in Figs. 5j and 5k, some fatigue cracks were found to be initiated at inclusions. This field of view indicates that inclusions facilitate the appearance of micro-cracks which disrupt inter-grain cohesion.

Fig. 6 shows a crack in the vicinity of the fracture surface at a distance of about 200 μm. Fig. 6a–d have the same magnification (the scale is shown in Fig. 6d). Scanning electron microscopy (SEM) imaging shows a panorama of the crack. The crack length is approximately 80 μm (Fig. 6a). The upper half of the crack (crack tip 2) is wider than lower half of the crack (crack tip 1) and the widest is about 5 μm. The crack tip 2 is considered to crack early. The propagating direction of the crack is 45°–60° to the tensile direction. The Inverse Pole Figure (IPF) map suggests that the crack is not affected by the molten pool boundary (Fig. 6b). The KAM values around the crack are high, which means that plastic deformation occurred before cracking (Fig. 6c). The proportion of KAM of deformed CX stainless steel less than 1° was 32 %, and the average KAM value was 1.24°. A low Taylor factor means that slip is more difficult than at a high Taylor factor. That is, plasticity requires a higher applied stress. Cracks usually propagate more slowly in regions with better plasticity (low Taylor factor). The small curvature of crack tip 2 is more likely due to unequal Taylor factors on either side of the crack tip region (Fig. 6d).

Fig. 6e and f are higher magnification images of the rectangular region in Fig. 6a. Black and grey lines represent high-angle (>15°)
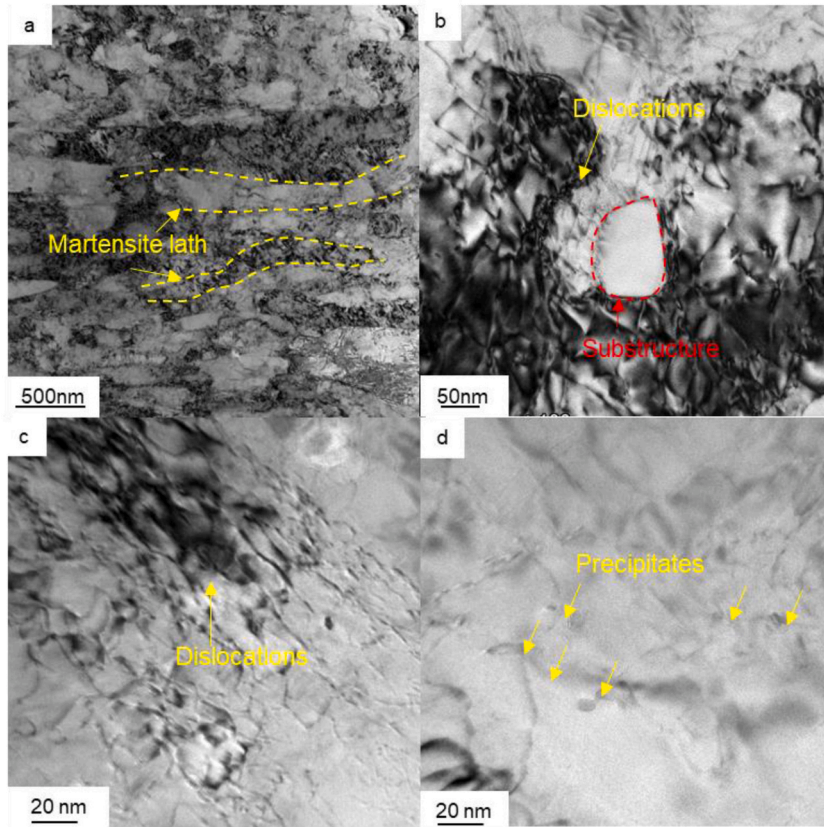
Fig. 3. TEM images of the SLM CX stainless steel: (a) Martensite lath; (b) Substructure; (c)Dislocations; (d) Precipitates.
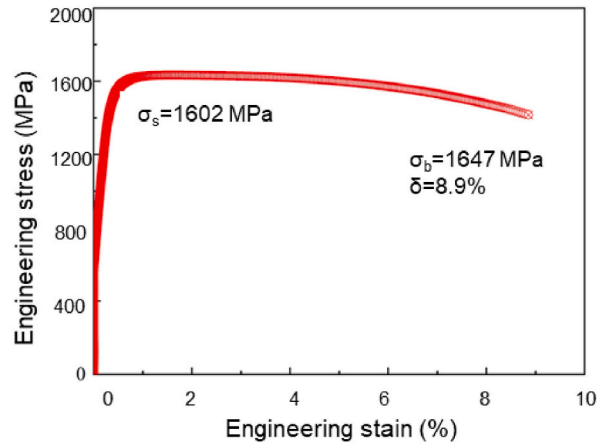

Fig. 4. Stress-strain curve of SLM CX stainless steel.

and low-angle (2–15°) grain boundaries, respectively. Ahead of crack tip 1, the orientations of the two narrow regions, as indicated by the two arrows, are different from the surrounding matrix, indicating that plastic deformation occurred before cracking. This is consistent with the high KAM values (Fig. 6c) and the large number of low-angle grain boundaries (Fig. 6e) around the crack. The orientations of the matrix on both sides of the crack are highlighted by cubes (Fig. 6f). Interestingly, the misorientation angles on the four positions are 5–13°. The matrix on both sides of the crack originally belonged to the same martensitic grains. The cracking in this region is therefore transgranular.

In Fig. 7a, the crack is approximately 12 μm long and 2 μm wide. The crack propagates at an angle of about 45° to the tensile direction. Grains around the upper crack tip with lower curvature are fine grains (Fig. 7b). For the matrix on either side of the upper
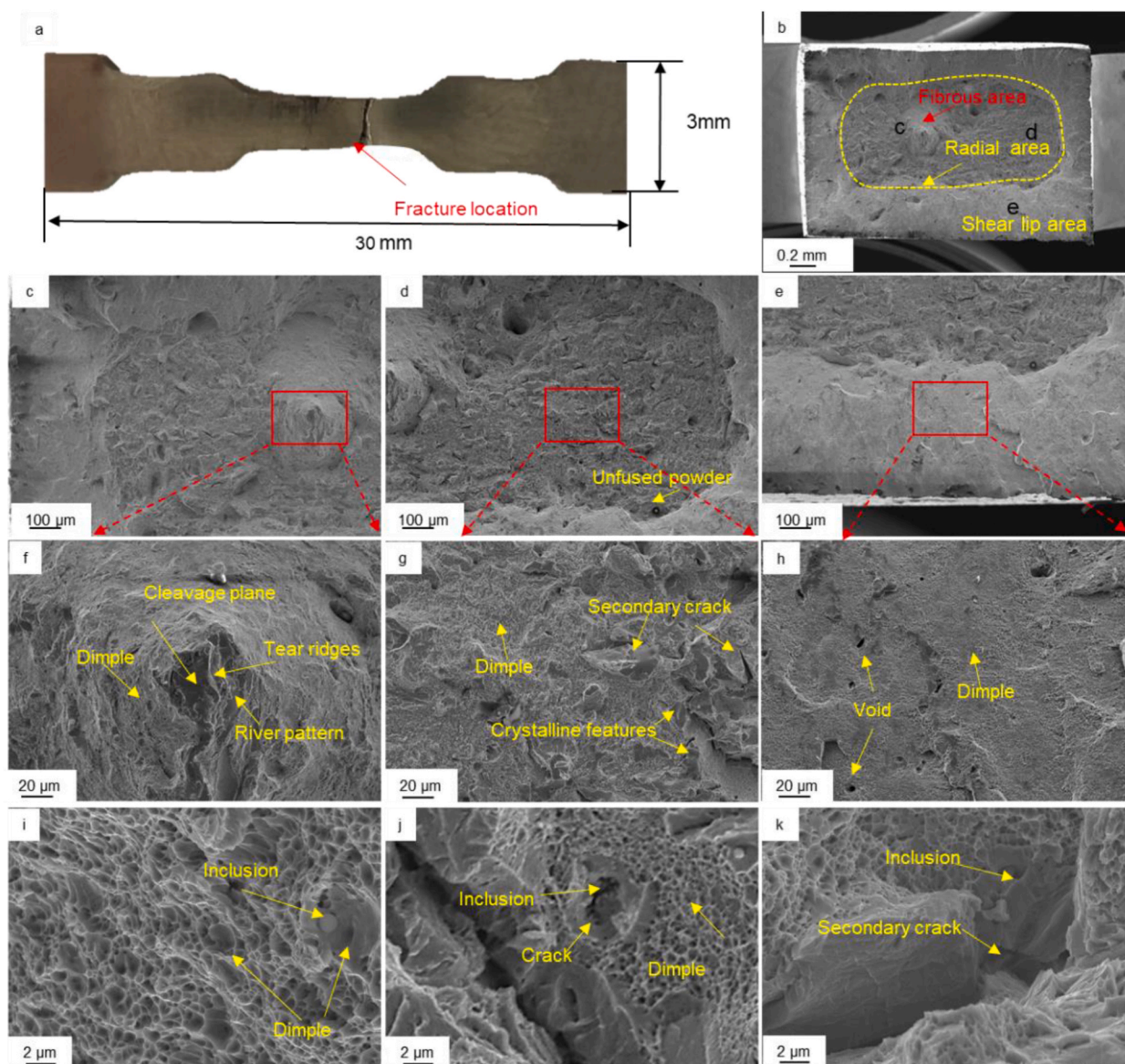
Fig. 5. Fractographies of the tensile sample: (a) Macroscopic appearance; (b) Fracture surface; (c, f) Fracture morphology in fibrous area; (d, g) Fracture morphology in radial area; (e, h) Fracture morphology in shear lip area; (i, j, k) Inclusions.

and lower crack tips, the misorientation angles are 23° and 52°, respectively, indicating that this crack propagated between grains. KAM values are higher around the upper crack tip (Fig. 7c), and Taylor factor values are low (Fig. 7d). The Taylor factor values in the region where the crack deflects (lower right side of the crack) are also low. This suggests that, as the crack propagated from a wider section downwards, cracking became more difficult when it encountered a region with a low Taylor factor. Fig. 7e shows the tip of another crack where its propagation direction is about 45° to the tensile direction, which is similar to the results in Fig. 6a. Based on the IPF map (Fig. 7f), a misorientation angle of 49° was measured between matrices on both sides of the crack, indicating that this crack is located between two grains.

The particle shown in Fig. 8 has debonded from the matrix, resulting in an ellipsoidal void opening that appears to have expanded through plastic deformation. The small cavity was tilted in the tensile direction. The matrix on the left upper and right lower sides of the particle has fewer low-angle grain boundaries (Fig. 8b). On the upper right side of the particle where the Taylor factor value is low, it can be seen that there is still a connection between the matrix and particle (Fig. 8d). This particular particle is rich in Al and O but poor in Cr and Fe as illustrated by Fig. 8e–h, suggesting it is an alumina inclusion. Due to its high hardness and large size, the inclusion did not deform during tension, resulting in stress concentration and separation from the matrix and serve as the crack nucleation sites, which is confirmed by Fig. 5. Clearly, improving the purity of CX stainless steel is crucial to its ductility.

The morphology of a region with pores is shown in Fig. 9, which displays a "peninsula" between two pores. The IPF image confirms
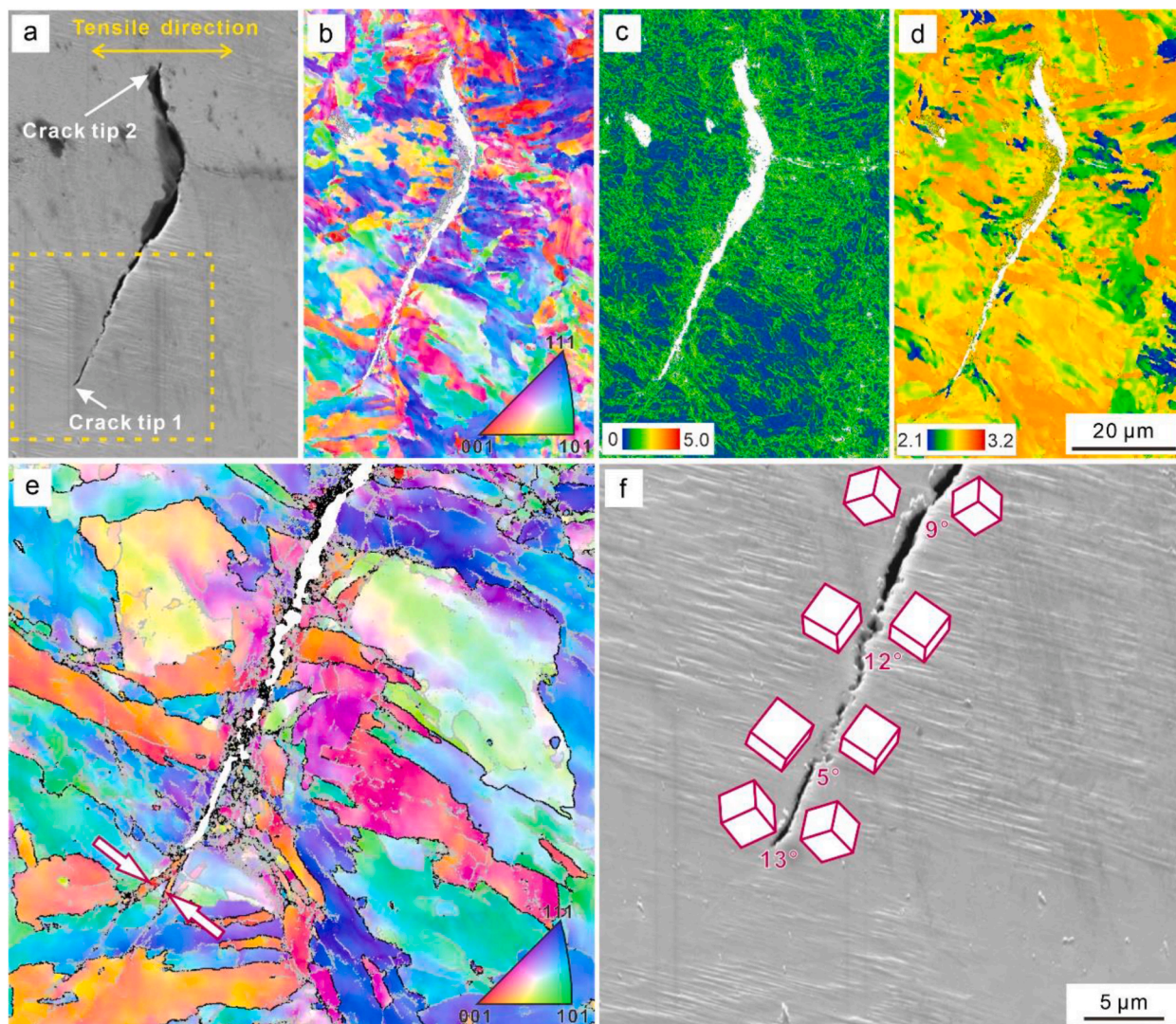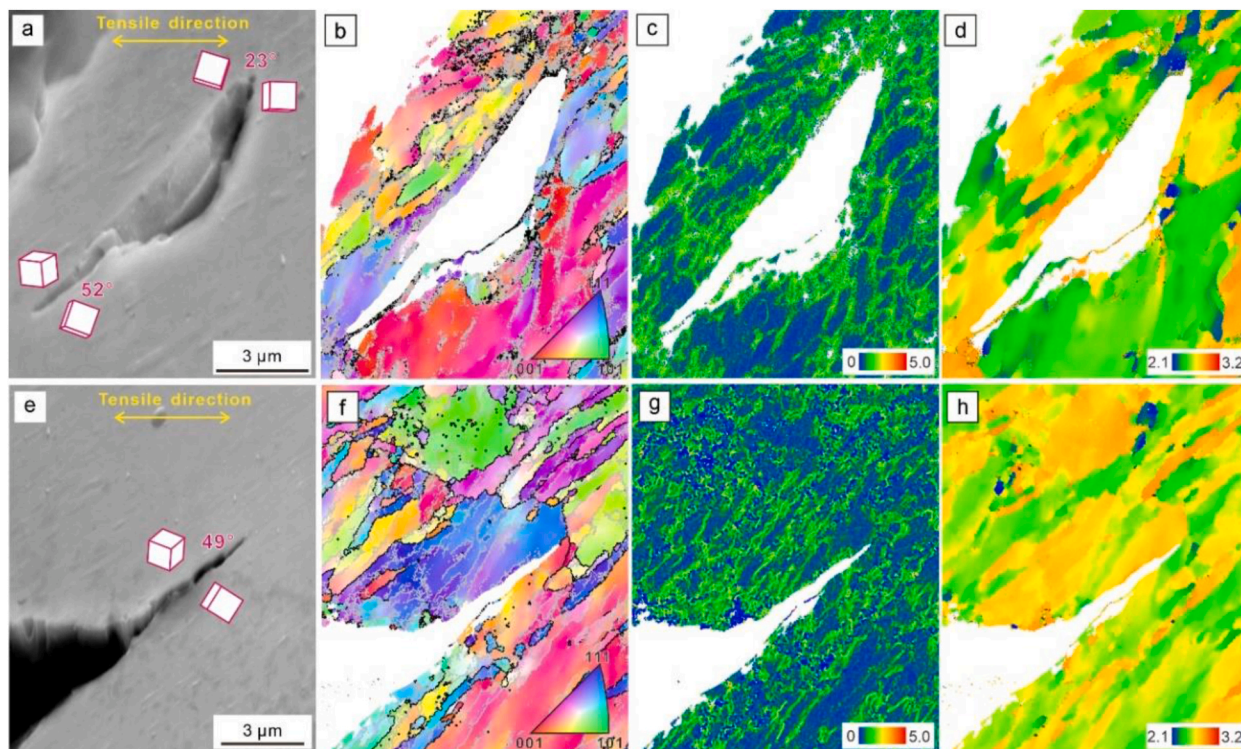
Fig. 6. Crack in the vicinity of the fracture surface (region 1): (a) SEM image; (b), (c), and (d) the corresponding IPF, KAM, and Taylor factor images; (e) Corresponding IPF map of the rectangular region in Fig. 6a; (f) SEM image corresponding to Fig. 6e.

that this "peninsula" is part of the matrix rather than an inclusion by showing its crystal orientation and grain boundaries (Fig. 9b). Pores and peninsulae are caused by incomplete fusion. This is consistent with the presence of unfused powder on fracture surfaces in additive manufactured CX steel [14]. The KAM value in the "peninsula" region is much lower than other regions, indicating non-significant plastic deformation under tension (Fig. 9c). Such pores, even at the micron level, disrupt the continuity of the matrix and can serve as crack initiation sites [20,21]. Hence, improving the density of the printed parts is also conducive to reducing the generation of crack sources.

4. Discussion

The fracture mechanism of SLM CX stainless steel was investigated by examining the fracture surfaces of tensile samples (Fig. 10). During the fracturing process, voids formed under the action of axial force, and these voids uniformly expanded in all directions and interconnected to create larger diameter dimples, enhancing the microzone's plasticity. During the tensile process, defects such as precipitates, inclusions, and unfused powders were separated from the matrix, leading to uneven plastic deformation. Voids and microcracks originated and grew at the defects. Several microcracks were interconnected and developed into major cracks as the deformation continued, leading to rapid destruction of CX stainless steel. Therefore, controlling the defects and nucleation of cracks is key to improving the plasticity of SLM CX stainless steel.

Compared to the KAM data of the undeformed CX stainless steel, the KAM values of CX stainless steel after tensile fracture varied, and the proportion of KAM >1° increased. KAM reflects the degree of uniformity of plastic deformation and dislocation density. A

Fig. 7. Crack in the vicinity of fracture surface (region 2 and 3): (a) SEM image of region 2; (b), (c), and (d) the corresponding IPF, KAM, and Taylor factor images; (e) SEM image of region 3; (f), (g), and (h) the corresponding IPF, KAM, and Taylor factor images.
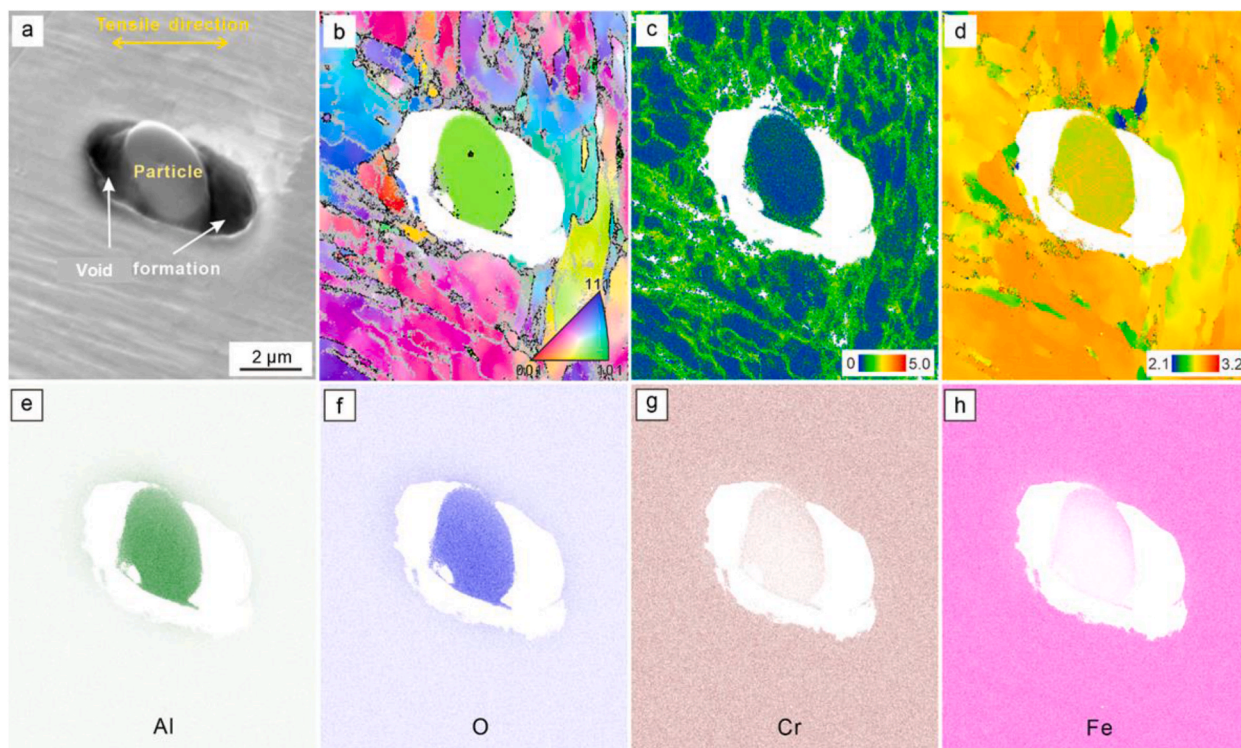
Fig. 8. Void opening at an inclusion: (a) SEM image; (b) IPF image; (c) KAM image; (d) Taylor factor image; (e)–(h) Element distribution images.
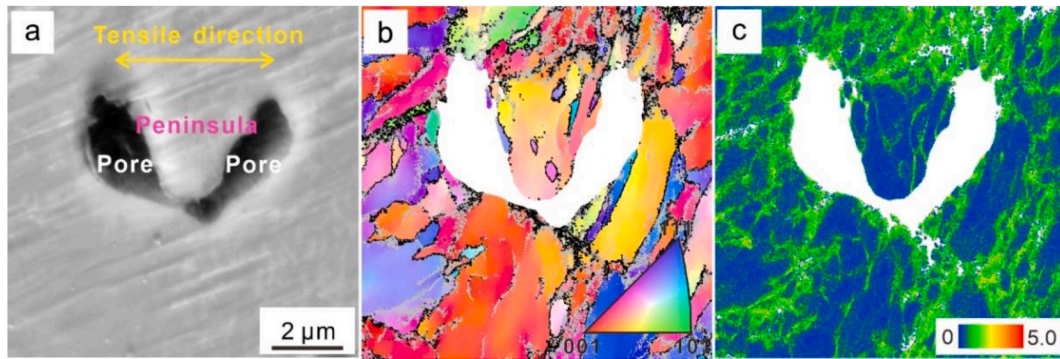
Fig. 9. Morphology of a region with pores: (a) SEM image; (b) IPF image; (c) KAM image.
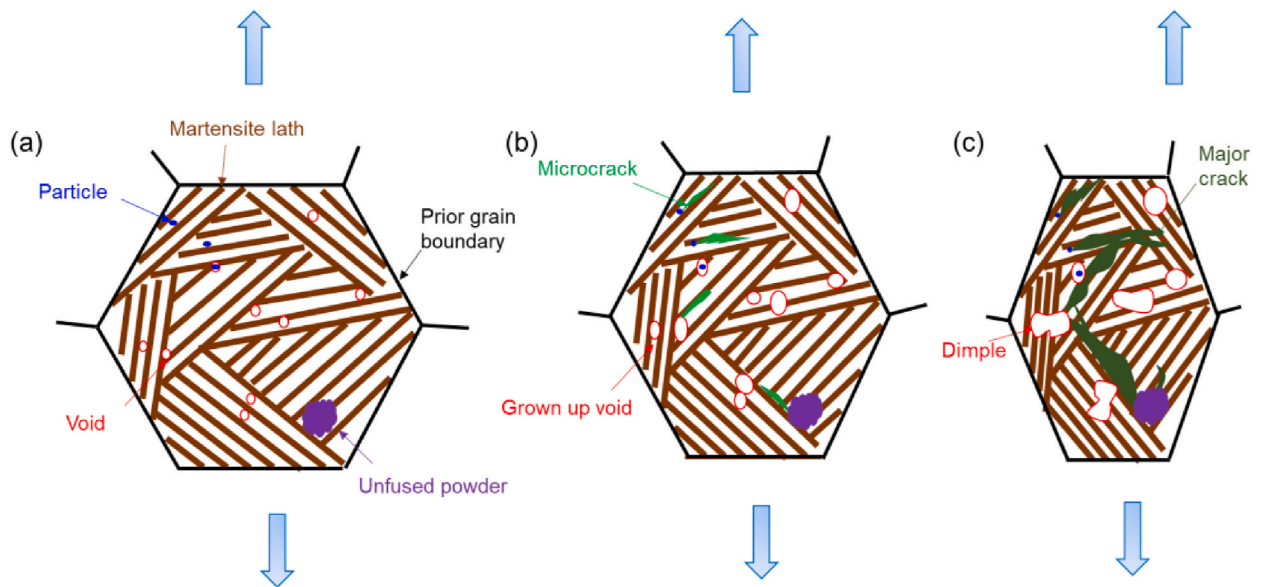

Fig. 10. Schematics of crack propagation for SLM CX stainless steel.

higher value indicates greater deformation-induced inhomogeneity and a more complex substructure. SLM CX stainless steel with non-uniform inclusions and substructures leads to a non-uniform distribution of local plastic strain and stress concentration. As a result, low-density and non-uniform micro-voids were formed, leading to stress concentration and martensite micro-cracking. As a result, the elongation of SLM CX stainless steel with high-density dislocations and substructures is relatively low.

5. Conclusion

In this work, the microstructure of SLM CX stainless steel is mainly martensitic lath with high density dislocations and dispersed precipitates, which contributes to its high strength. CX stainless steel was tensile tested to fracture and cracks in the vicinity of the fracture surface were analyzed by SEM and EBSD. Primary conclusions drawn from this work are listed as follows:

(1) The crack propagation direction is 45–60° to the tensile direction. Some cracks were transgranular, and some were intergranular. High-angle grain boundaries have little effect on crack propagation.
(2) The KAM values on both sides of the crack were higher than in other areas, indicating greater deformation-induced inhomogeneity. Regions with low Taylor factors inhibit crack propagation, resulting in crack tips with low curvature or even crack deflection.
(3) Inclusions and unfused powders can easily serve as crack nucleation sites. The plastic improvement of CX stainless steel requires the control of defects in SLM printed parts.

Funding statement

Data availability statement

The data that support the findings of this study are available on request from the corresponding author.

CRediT authorship contribution statement

Xiaojie Zhao: Writing – original draft, Investigation, Formal analysis, Data curation. **Yang Gao:** Methodology, Funding acquisition. **Kai Zhao:** Writing – review & editing, Formal analysis. **He Liu:** Resources, Methodology, Funding acquisition.

Declaration of competing interest

The authors declare that they have no known competing financial interests or personal relationships that could have appeared to influence the work reported in this paper.

References

[1] Ayda Shahriari, Ladan Khaksar, Nasiri Ali, Amir Hadadzadeh, Babak Shalchi Amirkhiz, Mohsen Mohammadi, Microstructure and corrosion behavior of a novel additively manufactured maraging stainless steel, Electrochim. Acta 339 (2020) 135925, https://doi.org/10.1016/j.electacta.2020.135925.

[2] Cheng Chang, Xingchen Yan, Rodolphe Bolot, Julien Gardan, Shuohong Gao, Min Liu, Hanlin Liao, Mahdi Chemkhi, Sihao Deng, Influence of post-heat treatments on the mechanical properties of CX stainless steel fabricated by selective laser melting, J. Mater. Sci. 55 (2020) 8303–8316, https://doi.org/10.1007/s10853-020-04566-x.

[3] Zhen Lu, Chengcai Zhang, Ruirui Fang, Hongbin Zhang, Haiping Zhou, Nana Deng, Zhenzhen Guo, Lianwang Gu, Microstructure evolution and corrosion behavior of the novel maraging stainless steel manufactured by selective laser melting, Mater. Char. 190 (2022) 112078, https://doi.org/10.1016/j.matchar.2022.112078.

[4] Ayda Shahriari, Mahya Ghaffari, Ladan Khaksar, Nasiri Ali, Amir Hadadzadeh, Babak Shalchi Amirkhiz, Mohsen Mohammadi, Corrosion resistance of 13wt.% Cr martensitic stainless steels: additively manufactured CX versus wrought Ni-containing AISI 420, Corrosion Sci. 184 (2021) 109362, https://doi.org/10.1016/j.corsci.2021.109362.

[5] Richard Fabian, Amir Hadadzadeh, Breaking strength-ductility trade-off in laser-powder bed fused Fe-Cr-Ni-Al maraging stainless steel: Controlled precipitation and preserved dislocation, Mater. Sci. Eng., A 868 (2023) 144761, https://doi.org/10.1016/j.msea.2023.144761.

[6] Cheng Chang, Xingchen Yan, Zhaoyang Deng, Bingwen Lu, Rodolphe Bolot, Julien Gardan, Sihao Deng, Mahdi Chemkhi, Min Liu, Hanlin Liao, Heat treatment induced microstructural evolution, oxidation behavior and tribological properties of Fe-12Cr-9Ni-2Al steel (CX steel) prepared using selective laser melting, Surf. Coating. Technol. 429 (2022) 127982, https://doi.org/10.1016/j.surfcoat.2021.127982.

[7] Shahriar Afkhami, Vahid Javaheri, Lipiäinen a Kalle, Amraei c Mohsen, Dabiri a dEdris, Timo Björk, Fatigue performance of stainless tool steel CX processed by laser powder bed fusion, Mater. Sci. Eng., A 841 (2022) 143031, https://doi.org/10.1016/j.msea.2022.143031.

[8] Ming-Hsiang Ku, Kai Ni, Quiao-En Lin, Shih-Hsien Chang, Ta-Wei Hsu, Chien-Lun Li, Chih-Kai Wang, Ming-Wei Wu, Novel laser powder bed fusion Corrax maraging stainless steel lattice with superior specific strength and energy absorption, J. Mater. Res. Technol. 25 (2023) 5240–5248, https://doi.org/10.1016/j.jmrt.2023.07.027.

[9] M.J. Benoit, S. Tabaie, T. Waqar, T. Ganton, B.S. Amirkhiz, A. Hadadzadeh, A. Nasiri, Effect of additive manufacturing process and isothermal aging on the microstructure and properties of 13-8 Mo precipitation hardening martensitic stainless steel, Addit. Manuf. 72 (2023) 103615, https://doi.org/10.1016/j.addma.2023.103615.

[10] Mehdi Sanjari, Amir Hadadzadeh, Hadi Pirgazi, Ayda Shahriari, Babak Shalchi Amirkhiz, Leo A.I. Kestens, Mohsen Mohammadi, Selective laser melted stainless steel CX: Role of built orientation on microstructure and micro-mechanical properties, Mater. Sci. Eng., A 786 (2020) 139365, https://doi.org/10.1016/j.msea.2020.139365.

[11] Hadi Pirgazi, Mehdi Sanjari, Saeed Tamimi, Babak Shalchi Amirkhiz, Leo A.I. Kestens, Mohsen Mohammadi, Texture evolution in selective laser melted maraging stainless steel CX with martensitic transformation, J. Mater. Sci. 56 (2021) 844–853, https://doi.org/10.1007/s10853-020-05290-2.

[12] Cheng Chang, Xingchen Yah, Zhaoyang Deng, Qingkun Chu, Sihao Deng, Rodolphe Bolot, Mahdi Chemkhi, Min Liu, Hanlin Liao, Julien Gardan, Effect of heat treatment on residual stress and wear resistance of CX stainless steel manufactured by selective laser melting, Procedia CIRP 104 (2021) 738–743, https://doi.org/10.1016/j.procir.2021.11.124.

[13] Amir Hadadzadeh, Ayda Shahriari, Babak Shalchi Amirkhiz, Jian Li, Mohsen Mohanmmadi, Additive manufacturing of an Fe-Cr-Ni-Al maraging stainless steel: microstructure evolution, heat treatment, and strengthening mechanisms, Mater. Sci. Eng., A 787 (2020) 139470, https://doi.org/10.1016/j.msea.2020.139470.

[14] Fayaz Foroozmehr, Yves Verreman, Jianqiang Chen, Denis Thibault, Philippe Bocher, Effect of inclusion on fracture behavior of cast and wrought 13% Cr-4% Ni martensitic stainless steels, Eng. Fract. Mech. 175 (2017) 262–278, https://doi.org/10.1016/j.engfracmech.2017.02.002.

[15] M.C. Niu, C.J. Chen, W. Li, K. Yang, J.H. Luan, W. Wang, Z.B. Jiao, Atomic-scale understanding of solute interaction effects on grain boundary segregation, precipitation, and fracture of ultrahigh-strength maraging steels, Acta Mater. 253 (2023) 118972, https://doi.org/10.1016/j.actamat.2023.118972.

[16] T. Tekin, G. Ischia, F. Naclerio, R. Ipek, A. Molinari, Effect of a direct aging heat treatment on the microstructure and the tensile properties of a 18Ni-300 maraging steel produced by laser powder bed fusion, Mater. Sci. Eng., A 872 (2023) 144921, https://doi.org/10.1016/j.msea.2023.144921.

[17] Hamed Asgari, Mohsen Mohammadi, Microstructure and mechanical properties of stainless steel CX manufactured by direct metal laser sintering, Mater. Sci. Eng., A 709 (2018) 82–89, https://doi.org/10.1016/j.msea.2017.10.045.

[18] Jiaqi Zhang, Minjie Wang, Liuhui Niu, Jianye Liu, Jinhai Wang, Yu Liu, Zhenwei Shi, Effect of process parameters and heat treatment on the properties of stainless steel CX fabricated by selective laser melting, J. Alloys Compd. 877 (2021) 160062, https://doi.org/10.1016/j.jallcom.2021.160062.

[19] Dongdong Dong, Chang Cheng, Hao Wang, Xingchen Yan, Wenyou Ma, Min Liu, Sihao Deng, Julien Gardan, Rodolphe Bolot, Hanlin Liao, Selective laser melting (SLM) of CX stainless steel: Theoretical calculation, process optimization and strengthening mechanism, J. Mater. Sci. Technol. 73 (2021) 151–164, https://doi.org/10.1016/j.jmst.2020.09.031.

[20] Mengzhen Cao, Yang Liu, Fionn P.E. Dunne,A crystal plasticity approach to understand fatigue response with respect to pores in additive manufactured aluminium alloys, Int. J. Fatig., 22, 61:106917. https://doi.org/10.1016/j.ijfatigue.2022.106917.

[21] Zhongji Sun, Yan Ma, Dirk Ponge, Stefan Zaefferer, Eric A. Jägle, Baptiste Gault, Anthony D. Rollett, Dierk Raabe, Thermodynamics-guided alloy and process design for additive manufacturing, Nat. Commun. 4361 (2022), https://doi.org/10.1038/s41467-022-31969-y.